

# Model Hamiltonian parameters for half-metallic ferromagnets NiMnSb and CrO<sub>2</sub>

A. Yamasaki,<sup>1,\*</sup> L. Chioncel,<sup>2,3</sup> A. I. Lichtenstein,<sup>4</sup> and O. K. Andersen<sup>1</sup>

<sup>1</sup>Max-Planck-Institut für Festkörperforschung Heisenbergstrasse 1, D-70569 Stuttgart, Germany

<sup>2</sup>Department of Physics, University of Oradea, 410087 Oradea, Romania

<sup>3</sup>Institute for Theoretical Physics and Computational Physics,  
Graz University of Technology, A-8010 Graz, Austria

<sup>4</sup>Institute of Theoretical Physics, University of Hamburg, Germany

(Dated: Received 10 March 2006; revised manuscript received 25 May 2006)

Using the recently developed  $N$ th-order muffin-tin-orbital (NMTO) based downfolding technique we revisit the electronic properties of half-metallic ferromagnets, the semi-Heusler NiMnSb and rutile CrO<sub>2</sub>. The NMTO Wannier orbitals for the Mn- $d$  and Cr- $t_{2g}$  manifolds are constructed and the mechanism of chemical bonding is discussed. The effective hopping Hamiltonian parameters are calculated using a NMTO downfolded basis set. We propose model Hamiltonian parameters with possibly minimal basis sets for both half-metallic ferromagnetic alloys.

PACS numbers: 75.50.Cc, 71.10.-w, 71.20.Lp, 71.15.Ap

## I. INTRODUCTION

Half-metallic ferromagnets (HMF) such as the semi-Heusler NiMnSb or the rutile CrO<sub>2</sub> are a subject of strongly growing interest mainly due to their potential applications in spin-dependent electronics, so-called “spintronics.”<sup>1,2,3,4</sup> Concerning their electronic structure, half-metallic materials exhibit a gap in one spin channel and a normal metallic behavior for the opposite spin bands. This means that electrons at the Fermi level are 100% spin polarized. Much experimental effort is devoted to the semi-Heusler NiMnSb compound, although highly spin-polarized carrier injection has not yet been achieved. At low temperatures superconducting point contact measurements revealed a less than 50% polarization of valence electrons.<sup>5,6</sup> Similar values were obtained by spin resolved photoemission,<sup>7</sup> and more recently experiments using the synchrotron radiation showed at room temperature a 40% polarization at the Fermi level.<sup>8</sup> This discrepancy in comparison with the predicted half-metallic behavior is attributed to interface and surface effects. However, by a proper engineering, half-metallicity can be restored at surface/interfaces.<sup>9</sup> The experimental evidence for half-metallicity is stronger in CrO<sub>2</sub>: Andreev reflection,<sup>10</sup> superconducting tunneling,<sup>11</sup> photoemission,<sup>12</sup> and point-contact magnetoresistance,<sup>13</sup> all give values of polarization in the range 85–100 %. Keizer *et al.* have injected new excitement into the field of half metals, by reporting the existence of a spin triplet supercurrent through the strong ferromagnet CrO<sub>2</sub>.<sup>14</sup>

Future spin electronic devices based on HMF will probably be expected to work around and above room temperature, so one of the essential requirements is that these ferromagnets should have quite high Curie temperatures. Both NiMnSb ( $T_c=730$  K) and CrO<sub>2</sub> ( $T_c=400$  K) fulfill this requirement. A second essential requirement for using half-metallic materials in practical devices could be the understanding of finite-temperature behavior of spin polarization both from the experimental and the theoret-

ical point of view.

On the theoretical side, HMF have been strongly supported by first-principles calculations, based on density-functional theory.<sup>4</sup> These calculations offer a proper description of the ground state properties, and are usually performed for zero temperatures. One way to approach the finite temperature behavior is based on modeling the many-body interactions in the real material, therefore the evaluation of the model Hamiltonian parameters is required. These parameters constitute the starting point for a finite-temperature full many-body microscopic description. The local density approximation (LDA) electronic structure allows us to evaluate the effective hopping parameters, to which a Hubbard type interaction is added to construct the starting Hamiltonian. In the multiorbital case the Hubbard Hamiltonian is described by

$$\hat{H}^{\text{int}} = \frac{1}{2} \sum_{imm',\sigma} U_{mm'} \hat{n}_{im\sigma} \hat{n}_{im'-\sigma} + \frac{1}{2} \sum_{imm'(\neq m),\sigma} (U_{mm'} - J_{mm'}) \hat{n}_{im\sigma} \hat{n}_{im'\sigma}, \quad (1)$$

where  $\sigma$  is the spin index,  $m, m'$  are local orbitals at site  $i$ . The on-site Coulomb interactions are expressed in terms of two parameters:  $U_{mm} = U$ ,  $U_{mm'(\neq m)} = U - 2J$ , and  $J_{mm'} = J$ .<sup>15</sup> This model Hamiltonian is defined on a basis set of local orbitals and thus the microscopic interactions are local, involving a small number of electrons and a small number of orbitals. A numerically exact solution of this model is achieved by the quantum Monte Carlo solver in the framework of the dynamical mean field theory (DMFT).<sup>16,17</sup> We used the recently developed LDA+DMFT methods<sup>15,18,19,20,21,22</sup> in order to investigate finite-temperature many-body effects for the practically important spintronic materials such as the semi-Heuslers NiMnSb,<sup>23</sup> FeMnSb,<sup>24</sup> and the zinc-blende CrAs (Ref. 25) and VAs.<sup>26</sup> In these materials, due to their half-metallic ferromagnetic band structure, the incoherent [nonquasiparticle (NQP)] states play an important

role. The NQP states were considered theoretically for the first time by Edwards and Hertz<sup>27</sup> in the framework of broad-band Hubbard model for itinerant electron ferromagnets.

For the realistic electronic structure of NiMnSb NQP states are situated just above the Fermi level for the minority spin channel, having a considerable spectral weight.<sup>23</sup> In FeMnSb the spectral weight of NQP states is enhanced in comparison with NiMnSb, producing a drastic depolarization at the Fermi level.<sup>24</sup> For CrAs in the zinc-blende structure,<sup>25</sup> the spectral weight of NQP states was studied in connection with the substrate lattice parameter. For large substrate lattice parameters the Fermi level is situated close to the middle of the minority spin gap and the NQP states are clearly visible. However, for smaller substrate lattice parameters the NQP contribution is negligible. VAs in a similar zinc-blende structure is predicted by LDA/GGA to be a narrow gap semiconductor.<sup>29</sup> In addition to the presence of NQP states, many-body interactions determine the closure of the semiconducting majority spin gap, leading to a half-metallic ferromagnetic ground state.<sup>26</sup> Therefore, a correct prediction of new spintronic materials should take into account finite-temperature many-body correlation effects, which might play an essential role in depolarization.

In order to further investigate the nature of the NQP state, a realistic model Hamiltonian is required. In this paper we will use the recently developed massive downfolding scheme<sup>30,31</sup> in order to produce real space Hamiltonian parameters for both NiMnSb and CrO<sub>2</sub> half-metallic compounds.

The paper is organized as follows. Section II describes briefly the computational details of the  $N$ th-order muffin-tin orbital (NMTO) method. The corresponding subsections II A and II B present the results of downfolding onto the Mn- $d$ , Cr- $t_{2g}$  manifolds, respectively, and gives the values of the effective hopping parameters. In the case of CrO<sub>2</sub> we compare the results of the matrix elements of the effective hopping Hamiltonian in two distinct Wannier orbitals basis sets: the one which describes the full Cr- $t_{2g}$  manifold and a second in which  $d_{xy}$  and  $d_{yz\pm zx}$  orbitals could be described individually. The values of the effective Coulomb interaction parameters are given in Sec. III. In the summary we discuss the construction of possible model Hamiltonians with a minimal basis set for both half-metallic ferromagnets.

## II. EFFECTIVE HOPPING PARAMETERS

In the present paper we use the NMTO method<sup>30,31</sup> for generation of localized Wannier functions. The NMTO method can be used to generate truly minimal basis sets with massive downfolding technique. Downfolding produces minimal bands which follows exactly the bands obtained with the large basis set. In the case of NiMnSb and CrO<sub>2</sub>, Mn- $d$  and Cr- $t_{2g}$  form the minimal basis set.

TABLE I: The muffin-tin radii for NiMnSb and CrO<sub>2</sub>. The radii of the empty spheres  $E$  are also given. The second row corresponds to the LMTO basis sets used in the self-consistent calculation of LDA potential. ( $l$ ) means that the  $l$ -partial waves were downfolded within the LMTO-ASA + cc.

$R_{\text{MT}}$ (a.u.)	NiMnSb			
	Ni	Mn	Sb	$E$
basis set	2.584	2.840	2.981	2.583
	$spd$	$spd$	$sp(df)$	$sp(d)$
$R_{\text{MT}}$ (a.u.)	CrO <sub>2</sub>			
	Cr	O	$E$	$E1$
basis set	2.213	2.094	1.653	1.566
	$spd$	$(s)p(d)$	$s(p)$	$s(p)$

The truly minimal set of symmetrically orthonormalized NMTOs is a set of Wannier functions. In the construction of the NMTO basis set the active channels are forced to be localized onto the eigenchannel  $\mathbf{R}lm$ , therefore the NMTO basis set is strongly localized.

Fourier transformation of the orthonormalized NMTO Hamiltonian,  $H^{\text{LDA}}(\mathbf{k})$ , yields on-site energies and hopping integrals,

$$H_{0m',\mathbf{R}m}^{\text{LDA}} \equiv \langle \chi_{0m'}^\perp | \mathcal{H}^{\text{LDA}} - \varepsilon_F | \chi_{\mathbf{R}m}^\perp \rangle \equiv t_{m',m}^{xyz}, \quad (2)$$

in a Wannier representation, where the NMTO Wannier function  $|\chi_{\mathbf{R}m}^\perp\rangle$  is orthonormal.

The matrix element between orbitals  $m'$  and  $m$ , both on site  $\mathbf{R}'=\mathbf{R}=0$ , is  $t_{m',m}^0$ , and the hopping integral from orbital  $m'$  on site  $\mathbf{R}'=0$  to orbital  $m$  on site  $\mathbf{R}=(x,y,z)$  is  $t_{m',m}^{xyz}$ .

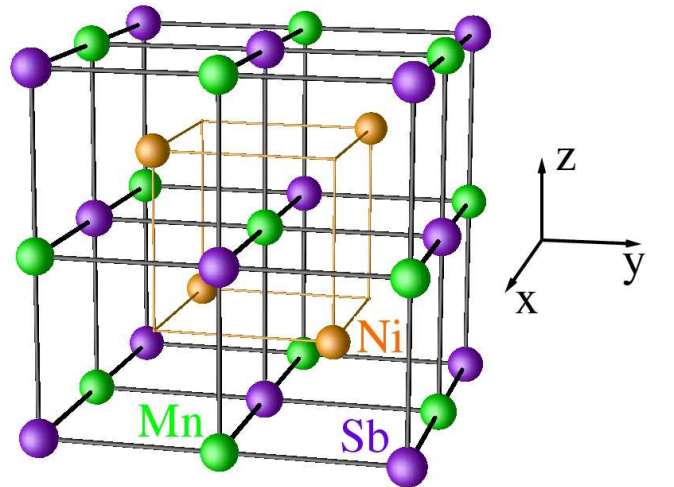


FIG. 1: (Color online)  $C1_b$  structure with the fcc Bravais lattice (space group  $F43m$ ). Mn (green) and Sb (purple) atoms are located at  $(0, 0, 0)$  and  $(\frac{1}{2}, \frac{1}{2}, \frac{1}{2})$  forming the rocksalt structure arrangement. Ni (orange) atom is located in the octahedrally coordinated pocket, at one of the cube center positions  $(\frac{3}{4}, \frac{3}{4}, \frac{3}{4})$  leaving the other  $(\frac{1}{4}, \frac{1}{4}, \frac{1}{4})$  empty. This creates voids in the structure.

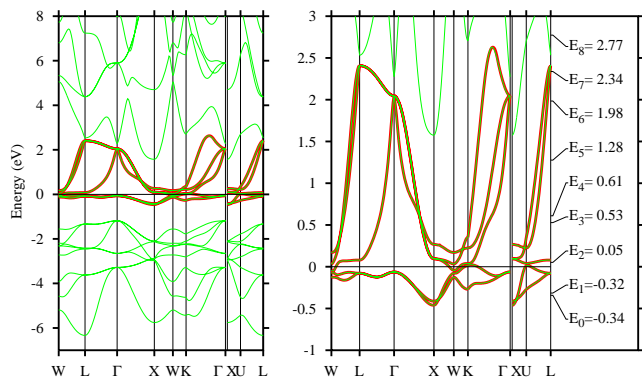


FIG. 2: (Color online) The band structure of non-spin-polarized NiMnSb calculated with the full basis is given in thick (green) line. The thin (red) band have been calculated with a Mn-*d* NMTO basis set. Fermi energy  $E_F$  is set to be zero. The high-symmetry points are  $W(\frac{1}{2}, 1, 0)$ ,  $L(\frac{1}{2}, \frac{1}{2}, \frac{1}{2})$ ,  $\Gamma(0, 0, 0)$ ,  $X(0, 1, 0)$ ,  $K(\frac{3}{4}, \frac{3}{4}, 0)$ , in the  $W$ - $L$ - $\Gamma$ - $X$ - $W$ - $K$ - $\Gamma$  line and  $X(0, 0, 1)$ ,  $U(\frac{1}{4}, \frac{1}{4}, 1)$ ,  $L(\frac{1}{2}, \frac{1}{2}, \frac{1}{2})$ , in the  $X$ - $U$ - $L$  line. Energy mesh used for downfolded calculation is given in the right of the band structure with a unit of eV.

The LDA potential is generated with the Stuttgart TB-LMTO-ASA code (the LMTO-ASA including the combined correction).<sup>32,33,34</sup> NMTO calculations are performed using the generated LDA potentials. The radii of MT potential spheres and the LMTO bases used in the calculation for NiMnSb and CrO<sub>2</sub> are listed in Table I. For the detail of the calculation, see the appendixes of Ref. [35].

#### A. Downfolding onto the Mn-*d* manifolds in NiMnSb

The intermetallic compound NiMnSb crystallizes in the cubic structure of MgAgAs type ( $C1_b$ ) with the fcc Bravais lattice (space group  $F\bar{4}3m = T_d^2$ ). The crystal structure is shown in Fig. 1. This structure can be described as three interpenetrating fcc lattices of Ni, Mn, and Sb. The Ni and Sb sublattices are shifted relative to the Mn sublattice by a quarter of the  $[111]$  diagonal in opposite directions. In the present calculation the experimental lattice constant of NiMnSb ( $a=5.927$  Å) is used.

A detailed description of the band structure of semi-Heusler alloys was given using electronic structure calculations and tight-binding model analysis,<sup>4,36,37,38,39</sup> and we briefly summarize the results. The key points, which determine the behavior of electrons near the Fermi level for the half-metallic property, are the interplay between the crystal structure, valence electron count, covalent bonding and large exchange splitting of the Mn-*d* electrons.

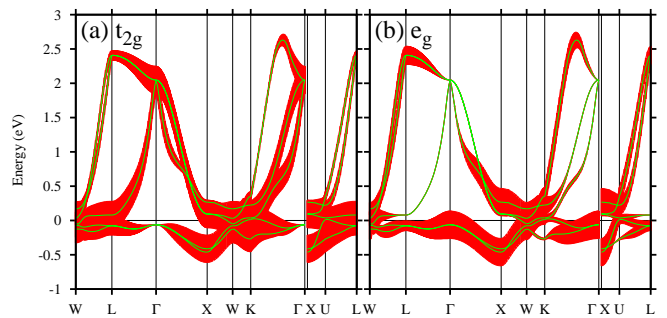


FIG. 3: (Color online) The NMTO band structure calculated with a Mn-*d* NMTO basis set. The bands have been decorated with (a)  $t_{2g}$  and (b)  $e_g$  characters. About symmetry points and  $E_F$ , see Fig. 2.

#### 1. Chemical bonding and the Mn-*d* Wannier orbitals

In the nonmagnetic phase the  $C1_b$  compounds have a *d-d* gap resulting from covalent hybridization of the higher-valent transition metal (Ni) with the lower-valent transition metal (Mn). For the minority spin gap opening, not only the Mn-*d*-Sb-*p* interactions, but also Mn-*d*-Ni-*d* interactions have to be taken into account. Moreover the loss of inversion symmetry produced by  $C1_b$  structure (the symmetry lowering from  $O_h$  in the  $L2_1$  structure to  $T_d$  in the  $C1_b$  structure at Mn site) is an essential additional ingredient. All the above interactions combined with the  $T_d$  symmetry lead to a nonzero anti-crossing of bands and to the gap opening. The existence of *sp*-valent Sb is crucial to provide stability to this compound.

Based on the understanding of the bonding in the NiMnSb, we propose a downfolding scheme in which all orbitals of all atoms except Mn-*d* is downfolded.

In Fig. 2 the non-spin-polarized band structure of NiMnSb is calculated with the full basis set (thick green line). Mn *d*, Ni *d*, and Sb *p* states are lying between  $-0.5$ – $2.5$  eV,  $-3$ – $-1$  eV, and  $-6.5$ – $-3$  eV, respectively. Sb *s* states are sitting around  $-12$ – $-10$  eV, that is not shown in Fig. 2. There is an excellent agreement with the previous calculations.<sup>4</sup> The thin red band has been calculated with the downfolded basis set which includes only Mn-*d* orbitals. The energy mesh used in the downfolded calculation is given to the right of the band structure. The two sets of bands are identical. In Fig. 3 the bandstructures of NiMnSb with the orbital character projected on to NMTO  $t_{2g}$  and  $e_g$  Wannier orbitals are shown. The fatness associated with each band is proportional to the character of the orbital. The strong hybridization between  $t_{2g}$  and  $e_g$  states is clearly seen. NMTO Mn-*d* Wannier orbitals are shown in Fig. 4. The triply degenerate manganese  $t_{2g}$  orbitals are very complicated due to the hybridization with Ni-*d* and Sb-*p* states. The  $d_{xy}$  orbital at Mn site is deformed by antibonding with the Ni-*d* state directed tetrahedrally to  $[11\bar{1}]$ ,  $[\bar{1}\bar{1}1]$ ,  $[1\bar{1}1]$ , and  $[\bar{1}11]$ . The same Ni-*d* orbitals couple with Sb-

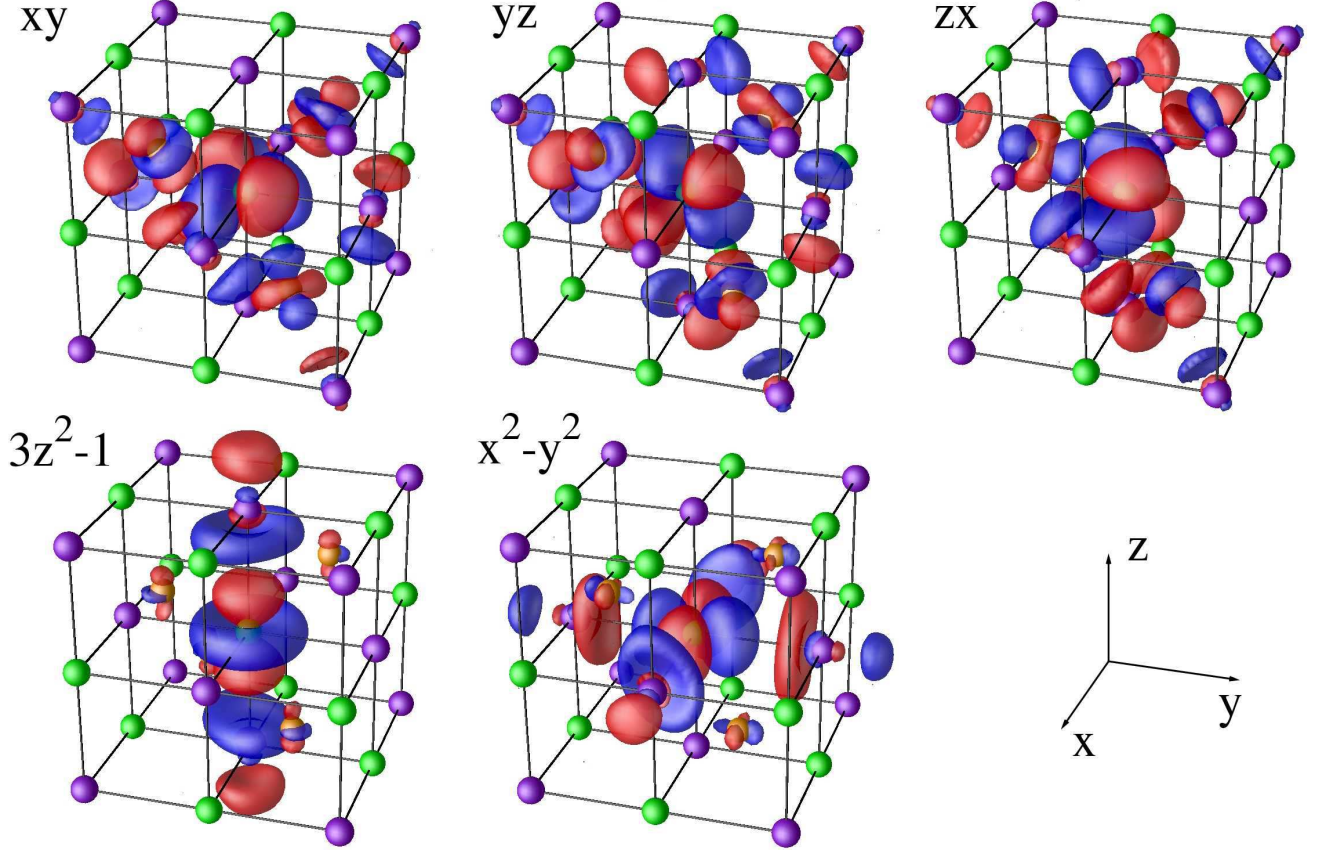


FIG. 4: (Color) NMT0 Mn- $d$  Wannier orbitals of NiMnSb. Ni is orange, Mn is green, and Sb is purple. Red (blue) indicates a positive (negative) sign. Upper panel:  $t_{2g}$  orbitals;  $d_{xy}$  (left),  $d_{yz}$  (middle),  $d_{zx}$  (right). The triply degenerate  $t_{2g}$  orbitals can be obtained by the permutation of axes. Lower panel:  $e_g$  orbitals;  $d_{3z^2-1}$  (left),  $d_{x^2-y^2}$  (middle). These  $e_g$  orbitals are doubly degenerated.

$p$  states. The direct Mn- $d_{xy}$ -Sb- $p$   $\pi$  coupling is not seen since the distance is  $d(\text{Mn-Sb}):d(\text{Ni-Sb})=1:\frac{\sqrt{3}}{2}$ . Therefore the Ni- $d$ -Sb- $p$  interactions are more favorable. The dispersion of the Mn  $t_{2g}$  bands is mainly due to hopping via the tails of Sb- $p$  and Ni- $d$  orbitals. On the other hand, the second nearest neighbor (NN)  $d$ - $d$  hopping of  $t_{2g}$  orbital is small. The  $e_g$  orbitals at Mn site are much easier to understand: they point towards Sb atoms, and a strong  $pd\sigma$  coupling between Sb- $p$  and Mn- $e_g$  states is seen. This induces large second NN  $d$ - $d$  hoppings.

## 2. Effective hopping matrix elements in the basis set of Mn- $d$ Wannier orbitals

In the many body picture the Mn  $t_{2g}$  and  $e_g$  constitutes the *active orbitals* which are responsible for the low energy physics, having fluctuation in occupation and spins. The effective hopping Hamiltonian matrix elements built up with these active orbitals are as follows.

NMT0 basis set:

$$|\chi^\perp\rangle = \{|xy\rangle, |yz\rangle, |zx\rangle, |3z^2-1\rangle, |x^2-y^2\rangle\}. \quad (3)$$

The on-site term:

$$t_{m',m}^{000} = \begin{pmatrix} 360 & 0 & 0 & 0 & 0 \\ 0 & 360 & 0 & 0 & 0 \\ 0 & 0 & 360 & 0 & 0 \\ 0 & 0 & 0 & 434 & 0 \\ 0 & 0 & 0 & 0 & 434 \end{pmatrix}. \quad (4)$$

The first nearest neighbor:

$$t_{m',m}^{0\frac{1}{2}\frac{1}{2}} = \begin{pmatrix} 129 & 2 & 23 & -100 & 12 \\ -2 & 51 & -2 & 75 & -130 \\ 23 & 2 & 129 & 40 & 92 \\ 100 & 75 & -40 & 9 & -37 \\ -12 & -130 & -92 & -37 & 51 \end{pmatrix}. \quad (5)$$

The second nearest neighbor:

$$t_{m',m}^{001} = \begin{pmatrix} -16 & 0 & 0 & -43 & 0 \\ 0 & -4 & 0 & 0 & 0 \\ 0 & 0 & -4 & 0 & 0 \\ 43 & 0 & 0 & -229 & 0 \\ 0 & 0 & 0 & 0 & -4 \end{pmatrix}, \quad (6)$$

where the unit is meV,  $E_F = 0$ , and hopping integrals up to the second NN are shown. The on-site term  $t_{m',m}^{000}$  is



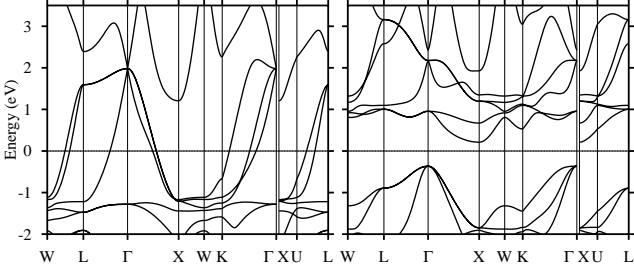


FIG. 5: Full basis set spin-polarized (ferromagnetic) bands for NiMnSb; majority spin (left) and minority spin (right). About symmetry points and  $E_F$ , see Fig. 2. The similarity of the spin-polarized majority with the non-spin-polarized bands is evidenced.

diagonal,  $t_{2g}$  and  $e_g$  orbitals are triply and doubly degenerated, respectively. The crystal-field splitting between  $t_{2g}$  and  $e_g$  orbitals is  $\sim 74$  meV. There are 12 first NN and 6 second NN hoppings. Only one hopping integral at each NN is shown, but all the hopping integrals can be derived from proper unitary transformation due to the crystal symmetry. For details, see Ref. [35]. The hopping between  $t_{2g}$  and  $e_g$  orbitals is strongly influenced by the presence of tails belonging to the Sb- $p$  and Ni- $d$  orbitals. Due to these tails large values of  $t_{2g}$  to  $e_g$  hoppings are evidenced in Eqs. (5) and (6). We mention that these hoppings should be small for the case of “pure”  $t_{2g}$  and  $e_g$  orbitals. In addition, due to the presence of Sb- $p$  and Ni- $d$  tails  $t_{2g}$  and  $e_g$  orbitals are not divided clearly as seen in Fig. 3. Therefore they should be treated equally. Hoppings further than third NN are small; for instance, the largest values are 66 (third) and 56 meV (fourth), a small number of matrix elements of the hoppings are less than  $\sim 30$  meV, and the others are almost zero in the third and fourth NN hoppings. Further NN hoppings are negligible.

In this procedure, we obtained the nonzero hopping matrix elements between the all Mn- $d$  orbitals, in the downfolded representation. The numbers of independent parameters of the effective model are equal to the number of matrix elements from Eqs. (4)–(6).

We now consider the spin-polarized case. Systems with 18 valence electrons per unit cell are semiconductors, but when they contain more than 18 electrons (22 electrons in NiMnSb, that is, Ni  $3d^8 4s^2$ , Mn  $3d^5 4s^2$ , and Sb  $5s^2 5p^3$ ), antibonding states are populated. Therefore, the non-magnetic phase becomes unstable and the magnetic state can be stabilized. The large exchange splitting of the Mn atom (producing a magnetic moment of around  $\sim 3.7 \mu_B$ ) is crucial to induce a half-metallic property. As we saw before, for the nonmagnetic case, the  $t_{2g}$  and  $e_g$  states of Ni are situated around 2 eV below  $E_F$ . In the spin-polarized calculation their position is slightly changed, therefore the exchange splitting on Ni is not large. The actual magnetic moment calculation gives a value around  $0.3 \mu_B$ .

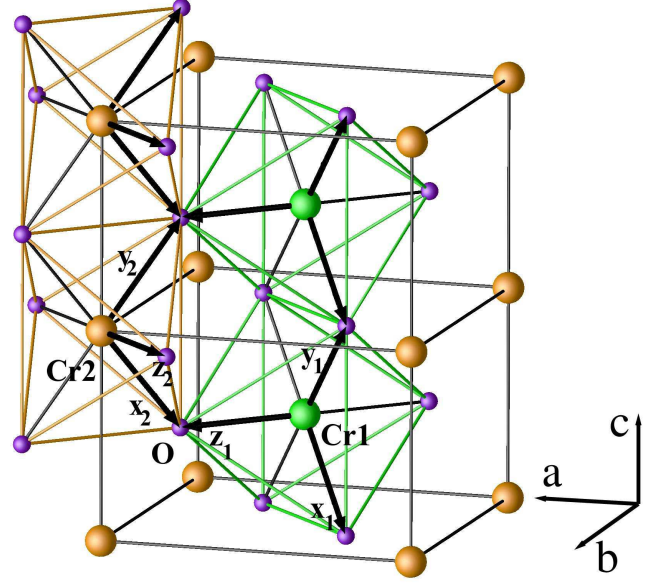


FIG. 6: (Color online) CrO<sub>2</sub> (rutile) structure. Cr1 (green) and Cr2 (orange) are located at  $(0, 0, 0)$  and  $(\frac{1}{2}, \frac{1}{2}, \frac{1}{2})$ . Cr atoms are octahedrally coordinated by oxygen atoms (purple). The local coordinate system is used for each Cr atom;  $\hat{x}_1 = -\frac{1}{2}\hat{a} + \frac{1}{2}\hat{b} - \frac{1}{\sqrt{2}}\hat{c}$ ,  $\hat{y}_1 = -\frac{1}{2}\hat{a} + \frac{1}{2}\hat{b} + \frac{1}{\sqrt{2}}\hat{c}$ ,  $\hat{z}_1 = \frac{1}{\sqrt{2}}\hat{a} + \frac{1}{\sqrt{2}}\hat{b}$ , and  $\hat{x}_2 = -\frac{1}{2}\hat{a} - \frac{1}{2}\hat{b} - \frac{1}{\sqrt{2}}\hat{c}$ ,  $\hat{y}_2 = -\frac{1}{2}\hat{a} - \frac{1}{2}\hat{b} + \frac{1}{\sqrt{2}}\hat{c}$ ,  $\hat{z}_2 = -\frac{1}{\sqrt{2}}\hat{a} + \frac{1}{\sqrt{2}}\hat{b}$ .  $\hat{x}_{1,2}$  and  $\hat{y}_{1,2}$  are approximately point to O atom, and  $\hat{z}_{1,2}$  are exactly point to O atom. The local axis is transformed into each other by a rotation of  $90^\circ$  around the crystal  $c$  axis.

The non-spin-polarized result has a striking resemblance to the majority spin-polarized calculations, presented in Fig. 5. Kulatov *et al.* explained half-metallicity of NiMnSb and CrO<sub>2</sub> by the extended Stoner factor calculations in the rigid-band approximation:<sup>39</sup> the minority spin-band gap opens due to the exchange splitting, which shifts minority bands, so they become empty. According to our results, the NMTO antibonding orbitals should be a good description for the empty Mn- $d$  states in the minority channel.

All the above results suggest that a minimal basis set which captures the essential physics in NiMnSb can be constructed using Mn  $t_{2g}$  and  $e_g$  states. Therefore, the non-spin-polarized result with Mn- $d$  orbitals can be a good starting point for the many-body calculations.

## B. Downfolding onto the Cr- $d$ manifolds in CrO<sub>2</sub>

Chromium dioxide CrO<sub>2</sub> has a rutile (tetragonal) structure with  $a=4.421$  Å,  $c=2.916$  Å ( $c/a=0.65958$ ), and internal parameter  $u=0.3053$ .<sup>40</sup> The Cr atoms form a body-center tetragonal lattice and are surrounded by a slightly distorted octahedron of oxygen atoms. The space group of this compound is nonsymmorphic ( $P4_2/mnm = D_{4h}^{14}$ ). Cr<sup>4+</sup> has a close shell Ar core and two additional

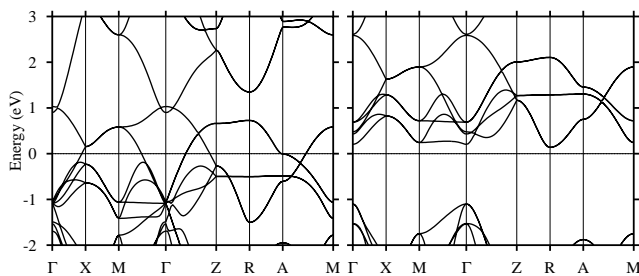


FIG. 7: Full basis set spin-polarized (ferromagnetic) bands for  $\text{CrO}_2$ ; majority spin (left) and minority spin (right).  $E_F$  is set to be zero. The high-symmetry points are  $\Gamma(0,0,0)$ ,  $X(0, \frac{1}{2}, 0)$ ,  $M(\frac{1}{2}, \frac{1}{2}, 0)$ ,  $Z(0, 0, \frac{1}{2})$ ,  $R(0, \frac{1}{2}, \frac{1}{2})$ ,  $A(\frac{1}{2}, \frac{1}{2}, \frac{1}{2})$ .

$3d$  electrons. The Cr ions are in the center of the  $\text{CrO}_6$  octahedra so the  $3d$  orbitals are split into a  $t_{2g}$  triplet and an excited  $e_g$  doublet. With only two  $3d$  electrons the  $e_g$  states are irrelevant and only the  $t_{2g}$  orbitals need to be considered. The tetragonal symmetry distorts the octahedra, which lifts the degeneracy of the  $t_{2g}$  orbitals into a  $d_{xy}$  ground state and  $d_{yz+zx}$  and  $d_{yz-zx}$  excited states,<sup>41,42</sup> where a *local coordinate system* is used for every octahedron (see Fig. 6). A double exchange mechanism for the two electrons per Cr site was proposed<sup>43</sup> in which due to the strong Hund's rule corroborated with the distortion of  $\text{CrO}_6$  octahedra leads to the localization of the one electron into the  $d_{xy}$  orbital, while the electrons in the  $d_{yz}$  and  $d_{xz}$  are itinerant.

Measurements of the magnetic susceptibility in the paramagnetic phase show a Curie-Weiss-like behavior indicating the presence of local moments,<sup>44</sup> suggesting a mechanism of ferromagnetism beyond the standard band or Stoner-like model.

Several recent experiments including photoemission,<sup>45</sup> soft x-ray absorption,<sup>46</sup> resistivity,<sup>47</sup> and optics<sup>48</sup> suggest that electron correlations are essential to the underlying physical picture in  $\text{CrO}_2$ . Schwarz<sup>49</sup> first predicted the half-metallic band structure with a spin moment of  $2\mu_B$  per formula unit for  $\text{CrO}_2$ . Later on Lewis<sup>41</sup> used the plane-wave potential method and investigated the energy bands and the transport properties, characterizing  $\text{CrO}_2$  as a “bad metal,” terminology applied to high temperature superconductors, or to the other transition metal oxides, even ferromagnets such as  $\text{SrRuO}_3$ . A decade later the LSDA+ $U$  calculation<sup>42</sup> explained the conductivity in the presence of large on-site Coulomb interactions, and concluded that  $\text{CrO}_2$  is a negative charge transfer gap material which leads to self-doping. Contrary to the on-site strong correlation description, transport and optical properties obtained within the FLAPW method (LSDA and GGA),<sup>50</sup> suggest that the electron-magnon scattering is responsible for the renormalization of the one-electron bands. In addition, more recent model calculations proposed even orbital correlations.<sup>51</sup>

### 1. Chemical bonding and the $\text{Cr-}t_{2g}$ Wannier orbitals

Chemical bonding in rutile-type compounds including  $\text{CrO}_2$  was analyzed by Sorantin and Schwarz.<sup>52</sup> Let us summarize their results: one can see that around the Fermi level, the bands are primarily chromium  $3d$  states of  $t_{2g}$  manifold, with  $e_g$  bands situated higher in energy due to the crystal-field splitting. In the spin polarized case, the exchange splitting shifts the minority spin- $d$  bands above the Fermi level, as seen in Fig. 7. For the majority  $t_{2g}$  bands the Fermi level is lying in a pseudo-gap. Oxygen  $p$ -chromium  $d$ , hybridization creates both bonding and antibonding hybrid orbitals, with the bonding orbital appearing in the occupied part and the antibonding hybrid orbital remaining in the Cr  $t_{2g}$  manifold. Half of the  $d_{yz}$  and  $d_{zx}$  components of  $t_{2g}$  are pushed upward, by antibonding, that explains the dominance of  $d_{xy}$  character in the spin density. The non-magnetic density of states shows a sharp peak at the Fermi level, which signals the magnetic instability according to the usual Stoner argument.

By the procedure of NMTOs we can easily gain a more complete picture about the chemical bonding. In Fig. 8 the non-spin-polarized band structure of  $\text{CrO}_2$  is calculated with the full basis set (thick green line). Cr  $e_g$ , Cr  $t_{2g}$ , and O  $p$  states are lying between 1.5–5 eV,  $-1$ –1.5 eV, and  $-7.5$ – $-1.5$  eV, respectively. There is an excellent agreement with the previous calculations.<sup>42,49,50,52</sup> The thin red bands have been calculated with the downfolded basis set which includes only Cr- $d$  orbitals. The energy mesh used in the downfolded calculation is given to the right of the band structure. NMTO Cr- $t_{2g}$  Wannier orbitals at Cr1  $(0, 0, 0)$  and Cr2  $(\frac{1}{2}, \frac{1}{2}, \frac{1}{2})$  are shown in Fig. 9. All  $t_{2g}$  orbitals form antibonding  $pd\pi$  coupling with O- $2p$  states. These antibonding NMTO Wannier orbitals capture the essentials to describe the half-

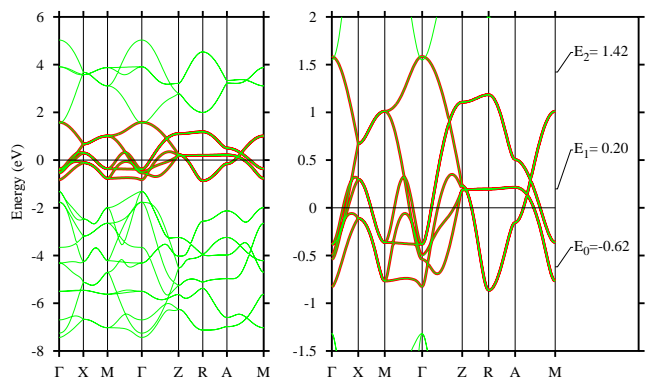


FIG. 8: (Color online) The band structure of non-spin-polarized  $\text{CrO}_2$  calculated with the full basis is given in thick (green) line. The thin (red) band have been calculated with a Cr- $t_{2g}$  NMTO basis set. Energy mesh used for downfolded calculation is given in the right of the band structure with a unit of eV. About symmetry points and  $E_F$ , see Fig. 7.

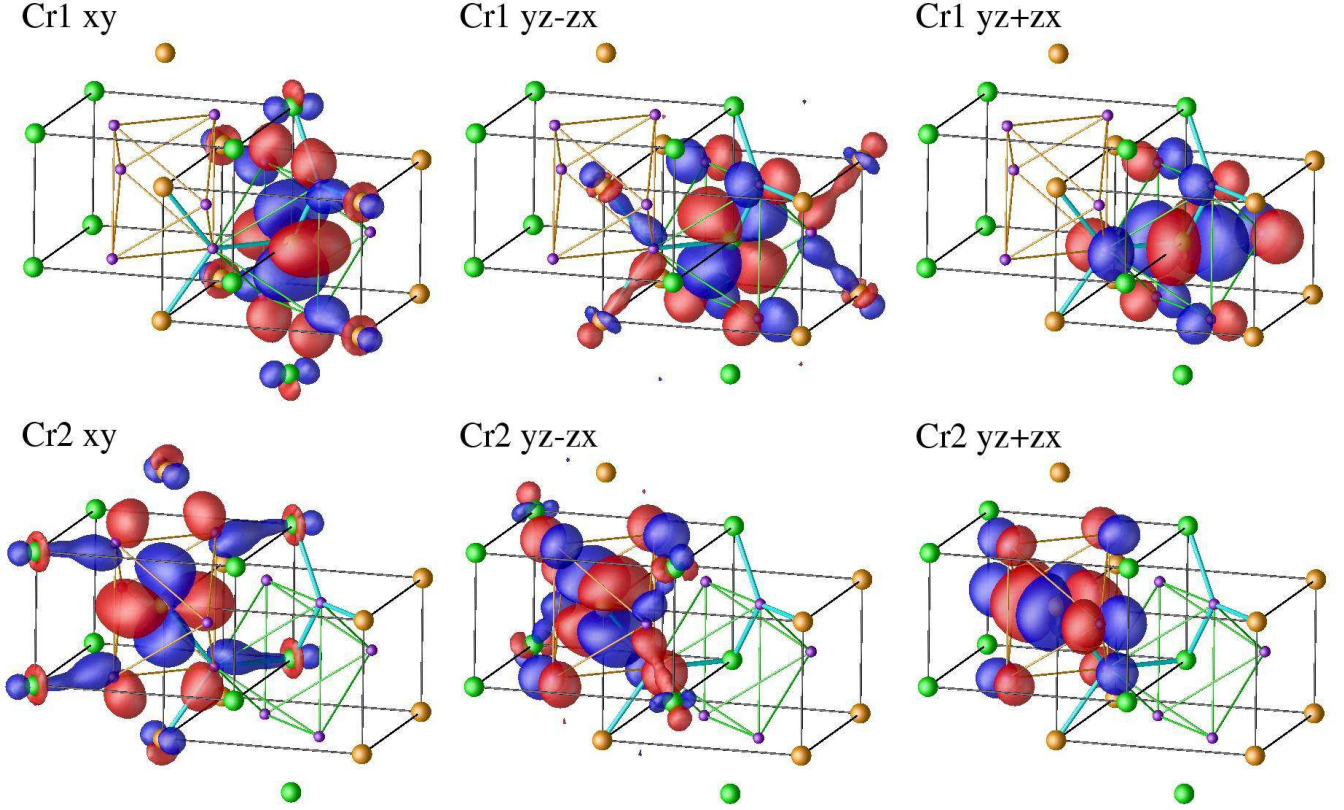


FIG. 9: (Color) NMTO Cr- $t_{2g}$  Wannier orbitals of  $\text{CrO}_2$ . Cr1 is orange, Cr2 is green, and O is purple. The local coordinate systems are used for each atom. Red (blue) indicates a positive (negative) sign. Upper panel: Cr1  $t_{2g}$  orbitals. Lower panel: Cr2  $t_{2g}$  orbitals.  $d_{xy}$  (left). This orbital is singly degenerated.  $d_{yz-zx}$  (middle) and  $d_{yz+zx}$  (right). These two orbitals are nearly degenerated.

metallicity of  $\text{CrO}_2$ .

Note that the local coordinate system is used.<sup>53</sup> For instance, the  $z$  axis at Cr1 site points along the  $[110]$ , while the  $z$  axis at Cr2 sites points towards the  $[\bar{1}10]$  direction. In the following we describe the essential features of the Cr- $d$  and O- $2p$  orbital couplings in the  $t_{2g}$  orbitals on Cr1 site:

(i)  $\text{Cr}_3\text{O}$  cluster. The oxygen atoms yield a  $\text{Cr}_3\text{O}$  cluster with three surrounding Cr atoms. The Cr1 atom has six  $\text{Cr}_3\text{O}$  clusters with two different types; for instance, one  $\text{Cr}_3\text{O}$  cluster is formed by Cr1 at  $(0,0,0)$  and  $(0,0,1)$ , Cr2 at  $(-\frac{1}{2}, \frac{1}{2}, \frac{1}{2})$ , and O at  $(u - \frac{1}{2}, \frac{1}{2} - u, \frac{1}{2})$  in the  $(110)$  plane. Another type of  $\text{Cr}_3\text{O}$  cluster is formed by Cr1 at  $(0,0,0)$ , Cr2 at  $(\frac{1}{2}, \frac{1}{2}, \pm\frac{1}{2})$ , and O at  $(u, u, 0)$  in the  $(\bar{1}10)$  plane. The O is sitting in the center of a triangle formed by the three coplanar Cr nearest atoms. The  $\text{Cr}_3\text{O}$  cluster is indicated by thick cyan lines in Fig. 9. In the  $\text{Cr}_3\text{O}$  unit, one can see one antibonding  $pd\pi$  coupling between Cr- $t_{2g}$  and O- $p$  states and two bonding  $pd\sigma$  couplings between Cr- $e_g$  and O- $p$  states. On one hand, the Cr- $e_g$  and Cr- $t_{2g}$  orbitals lying within the  $\text{Cr}_3\text{O}$  plane couple to the in-plane O- $p$  orbital. On the other hand, the out-of-plane O  $p$  orbital component, perpendicular to the  $\text{Cr}_3\text{O}$  plane, cannot couple to the Cr- $e_g$  state due to orthogonality.

(ii)  $d_{xy}$  orbitals. The Cr1 atom experiences a bonding coupling between its  $d_{xy}$  orbital and the  $e_g$  ( $d_{3z^2-1}$ ) orbital located on the other six nearest Cr atoms on the  $(110)$  plane via  $\text{Cr}_3\text{O}$  cluster. The bonding is realized via the tails of O- $2p$  ( $p_x$ - and  $p_y$ -like) orbitals.  $e_g$  tails belonging to the first NN Cr1  $(0,0,\pm 1)$  and second NN Cr2  $(-\frac{1}{2}, \frac{1}{2}, \pm\frac{1}{2})$ ,  $(\frac{1}{2}, -\frac{1}{2}, \pm\frac{1}{2})$  atoms are visible in the  $(110)$  plane, where the  $d_{xy}$  orbital is situated. Further, the  $d_{3z^2-1}$  state belonging to the Cr1  $(0,0,1)$  atom forms a  $pd\sigma$ -type bonding with both O  $p_x$  orbital located at  $(u - \frac{1}{2}, \frac{1}{2} - u, \frac{1}{2})$  and with O  $p_y$  situated at  $(\frac{1}{2} - u, u - \frac{1}{2}, \frac{1}{2})$ . The  $d_{xy}$  orbital, on the contrary, forms an antibonding coupling with these O  $p_x$  and O  $p_y$  states. Cr2 atom situated at  $(-\frac{1}{2}, \frac{1}{2}, \frac{1}{2})$  involves its  $d_{3z^2-1}$  orbital into a  $pd\sigma$  bonding with O  $p_x$  orbital situated at  $(u - \frac{1}{2}, \frac{1}{2} - u, \frac{1}{2})$ .

(iii)  $d_{yz-zx}$  orbitals. The O atoms situated at  $(u, u, 0)$  and  $(-u, -u, 0)$  intermediate a  $pd\sigma$  bonding, via their  $p_x$ - $y$  orbital, between the  $d_{yz-zx}$  orbital at Cr1  $(0,0,0)$  and the  $e_g$  orbitals at Cr2  $(\frac{1}{2}, \frac{1}{2}, \pm\frac{1}{2})$  and  $(-\frac{1}{2}, -\frac{1}{2}, \pm\frac{1}{2})$  atoms. This bonding orbital is situated in the  $(\bar{1}10)$  plane similarly to the  $d_{yz-zx}$  orbital. However, its bonding strength seems to be weaker than the ones of the  $d_{xy}$  orbitals, due to a larger distance between O and Cr2 atoms. The O  $p_z$  orbitals belonging to the atoms situated



at  $(\frac{1}{2} - u, u - \frac{1}{2}, \pm\frac{1}{2})$  and  $(u - \frac{1}{2}, \frac{1}{2} - u, \pm\frac{1}{2})$ , form a  $pd\pi$  coupling with  $d_{yz-zx}$  orbital. Therefore the O  $p_z$  orbital perpendicular to the plane of the  $\text{Cr}_3\text{O}$  cluster does not overlap with the  $e_g$  tails of Cr1  $(0,0,\pm1)$  atoms sitting along the  $[001]$  direction.

(iv)  $d_{yz+zx}$  orbitals. The  $e_g$  tails can not contribute at all to the  $d_{yz+zx}$  orbital. Because O  $p_z$  orbitals at  $(\frac{1}{2} - u, u - \frac{1}{2}, \pm\frac{1}{2})$ ,  $(u - \frac{1}{2}, \frac{1}{2} - u, \pm\frac{1}{2})$  and O  $p_{x+y}$  orbitals at  $(u, u, 0)$ ,  $(-u, -u, 0)$  are situated perpendicular to  $\text{Cr}_3\text{O}$  clusters, the coupling between O  $p$  ( $p_z$  and  $p_{x+y}$ ) states and  $e_g$  states at surrounding Cr atoms is not allowed due to the orthogonality.

We discussed in the above points (i)–(iv), the direct or mediated interactions between Cr- $d$  and O- $p$  or between the Cr  $t_{2g}$  and  $e_g$  states. As it is already known,<sup>42,49,50,52</sup> there is a significant difference between the  $t_{2g}$  and  $e_g$  orbitals, however the above analysis in the framework of NMTO technique shows that their interplay constitutes an important ingredient not only for the crystal-field splitting of  $t_{2g}$  states, but also for the general bonding in the rutile structure. The  $t_{2g}$  orbitals form the basis set in which the effective hopping Hamiltonian matrix elements are evaluated. These results are presented below.

## 2. Effective hopping matrix elements in the Cr- $t_{2g}$ Wannier orbitals

The hopping integrals  $t$  with  $t_{2g}$  Wannier representation up to the second NN are as follows.

NMTO basis set:

$$|\chi^\perp\rangle = \{|xy\rangle, |yz-zx\rangle, |yz+zx\rangle\}. \quad (7)$$

The on-site term:

$$t_{m',m}^{000} = \begin{pmatrix} 104 & 0 & 0 \\ 0 & 323 & 0 \\ 0 & 0 & 355 \end{pmatrix}. \quad (8)$$

The first nearest neighbor:

$$t_{m',m}^{001(\text{Cr1} \rightarrow \text{Cr1})} = \begin{pmatrix} -119 & 0 & 0 \\ 0 & -177 & 0 \\ 0 & 0 & 196 \end{pmatrix}. \quad (9)$$

The second nearest neighbor:

$$t_{m',m}^{\frac{1}{2}\frac{1}{2}\frac{1}{2}(\text{Cr1} \rightarrow \text{Cr2})} = \begin{pmatrix} -4 & 0 & 0 \\ 32 & 0 & 0 \\ 0 & -204 & 142 \end{pmatrix}, \quad (10)$$

where the unit is meV and a local coordinate system for each atom Cr1 and Cr2 in the unit cell is used as seen in Fig. 6. The on-site term  $t_{m',m}^{000}$  and the first NN hoppings are diagonal in a  $\{d_{xy}, d_{yz-zx}, d_{yz+zx}\}$  representation. The splitting between these orbitals is due partly to the orthorhombic distortion of  $\text{CrO}_6$  octahedra and partly to the bonding with the  $e_g$  states of nearest Cr atoms in rutile structure. As a consequence mainly two

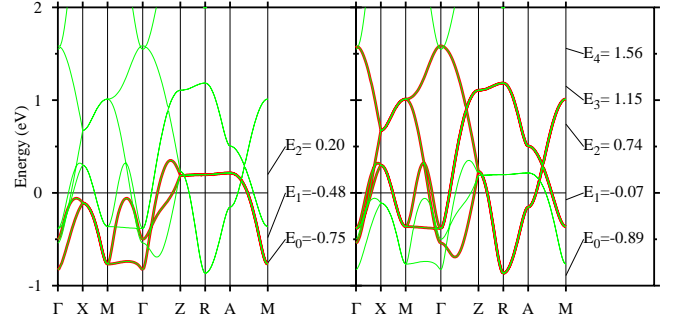


FIG. 10: (Color online) NMTO downfolded  $d_{xy}$  (left) and  $d_{yz\pm zx}$  (right) bands for  $\text{CrO}_2$ . Energy mesh used for each calculation is given in the right of the band structure with a unit of eV. For symmetry points and  $E_F$ , see Fig. 7.

crystal-field levels are formed, a single  $d_{xy}$  and two nearly degenerate  $d_{yz\pm zx}$  orbitals situated with  $\sim 235$  meV at higher energies, that can be derived from the difference between on-site levels of  $d_{xy}$  and  $d_{yz\pm zx}$  orbitals in Eq. (8). A possible ingredient in determining the position of the nearly degenerate  $d_{yz\pm zx}$  orbitals with respect to the single  $d_{xy}$  orbital is the bond length between Cr and O atoms. In the calculations presented in this paper a longer bond length along  $z$  direction ( $d_\perp = 1.91$  Å) is used in comparison with the bond formed in the  $xy$  plane having a value of ( $d_\parallel = 1.89$  Å). In another experiment, however, the opposite situation is reported,  $d_\perp = 1.89$  Å is smaller than  $d_\parallel = 1.91$  Å.<sup>54</sup> In both cases, however, the band structure and density of states are almost identical. Moreover other oxides ( $\text{TiO}_2$ ,  $\text{VO}_2$  etc.) with rutile structure have a similar band structure and density of states for  $t_{2g}$  states. This fact suggests that the bonding with  $e_g$  state is essential for the crystal-field splitting of  $t_{2g}$  states. Similar mechanism for the crystal-field splitting of  $t_{2g}$  state is realized in  $\text{V}_2\text{O}_3$  (Ref. 55) and  $\text{NaCoO}_2$ .<sup>56</sup>

There are two first NN between Cr1 (Cr2) and eight second NN hoppings between Cr1 and Cr2. Only one hopping integral at each NN is shown here. The hopping integrals are strongly affected by Wannier function's tails which are mainly due to downfolded O  $2p$  and Cr  $e_g$  orbitals.  $d_{xy}$  orbital has a small second nearest hopping integrals  $t_{xy,xy}^{\frac{1}{2}\frac{1}{2}\frac{1}{2}} = -4$  meV although O  $p$  tails are present. This means that  $d_{xy}$  orbital does not have the second NN hopping path, indicating a very narrow  $d_{xy}$  band. On contrary, large hopping integrals of the second NN are shown in  $d_{yz\pm zx}$  block.  $d_{yz+zx}$  orbitals can hop to  $d_{yz+zx}$  of all direction ( $|t_{yz+zx,yz+zx}^{2\text{nd NN}}| = 142$  meV), but  $d_{yz-zx}$  can not to  $d_{yz-zx}$  ( $t_{yz-zx,yz-zx}^{2\text{nd NN}} = 0$  meV exactly, as a consequence of orthogonality.) The hopping between  $d_{yz-zx}$  and  $d_{yz+zx}$  ( $|t| = 204$  meV) is allowed for a particular direction, that is, the second NN hopping from Cr1  $d_{yz+zx}$  to Cr2  $d_{yz-zx}$  sitting in  $(1\bar{1}0)$  plane or from Cr1  $d_{yz-zx}$  to Cr2  $d_{yz+zx}$  sitting in  $(110)$  plane. The large values of second NN hopping in  $d_{yz\pm zx}$  block are caused by O  $p$



tails which are not orthogonal to each other, and induce both the itinerant property and the wide band of  $d_{yz\pm zx}$  states.  $d_{yz\pm zx}$  orbitals have the second NN hopping path via O  $p$  tails. Moreover the large off-diagonal hopping integral of second NN and the small crystal-field splitting between  $d_{yz\pm zx}$  indicate that  $d_{yz\pm zx}$  states should be treated together. The Cr1  $d_{yz-zx}$  orbital is weakly coupled with Cr2  $d_{xy}$  ( $|t|=32$  meV) along particular directions, within the (110) plane. Hoppings towards the third NN are small; for instance, the largest values are 45 meV (third) and 30 meV (fourth and fifth), and the others are almost zero. Further away NN hoppings are much smaller.

Exceptions are, however, the  $e_g$  tails of Wannier function which gives a few large hopping integrals, for instance,  $t_{xy,xy}^{002(\text{Cr1}\rightarrow\text{Cr1})} = -82$  meV,  $t_{xy,xy}^{110(\text{Cr1}\rightarrow\text{Cr1})} = -95$  meV, and  $t_{yz-zx,yz-zx}^{11\frac{1}{2}(\text{Cr1}\rightarrow\text{Cr1})} = -50$  meV. These large hoppings can be seen in Fig. 9.

### 3. Effective hopping matrix elements in the independent $d_{xy}$ and $d_{yz\pm zx}$ Wannier orbitals

As seen in Eqs. (8)–(10), the coupling between  $d_{xy}$  and  $d_{yz\pm zx}$  seems to be weak. The NMTO method may be able to pick up such bands independently. The  $d_{xy}$  and  $d_{yz\pm zx}$  bands are shown in Fig. 10. The Wannier orbitals are more extended due to additional downfolding. This affects the hopping integrals as well. The hopping integrals  $\tilde{t}$  with  $d_{xy}$  and  $d_{yz\pm zx}$  Wannier representation up to the second NN are as follows.

NMTO basis set:

$$|\chi^\perp\rangle = \{ |xy\rangle, |yz-zx\rangle, |yz+zx\rangle \}. \quad (11)$$

The on-site term:

$$\tilde{t}_{m',m}^{000} = \begin{pmatrix} -24 & & \\ & 312 & 0 \\ & 0 & 373 \end{pmatrix}. \quad (12)$$

The first nearest neighbor:

$$\tilde{t}_{m',m}^{001(\text{Cr1}\rightarrow\text{Cr1})} = \begin{pmatrix} -99 & & \\ -187 & 0 & \\ & 0 & 197 \end{pmatrix}. \quad (13)$$

The second nearest neighbor:

$$\tilde{t}_{m',m}^{\frac{1}{2}\frac{1}{2}\frac{1}{2}(\text{Cr1}\rightarrow\text{Cr2})} = \begin{pmatrix} -26 & & \\ & 0 & 0 \\ & -202 & 135 \end{pmatrix}, \quad (14)$$

where the same definitions of Eqs. (7)–(10) are used. Since the Wannier orbitals are more extended the hoppings are modified slightly, but not changed significantly. A few large hoppings of far NN are also reduced;  $t_{xy,xy}^{002(\text{Cr1}\rightarrow\text{Cr1})} = -21$  meV,  $t_{xy,xy}^{110(\text{Cr1}\rightarrow\text{Cr1})} = -16$  meV, and  $t_{yz-zx,yz-zx}^{11\frac{1}{2}(\text{Cr1}\rightarrow\text{Cr1})} = -39$  meV. In addition, there is no

matrix elements in LDA Hamiltonian between  $d_{xy}$  and  $d_{yz\pm zx}$  block, that is there is no LDA interaction between them, by virtue of our construction of NMTO Wannier functions.

The possibly minimal set of Wannier function may provide new insights. At the first glance one can separate the narrow  $d_{xy}$  orbitals from the extended  $d_{yz\pm zx}$  states. The former would be treated as corelike (classical) spin  $S = 1/2$ , meanwhile in the later dispersive  $d_{yz\pm zx}$  bands the Coulomb repulsion would be treated in a usual quantum many-body way. Such a Kondo-lattice type model, for  $\text{CrO}_2$  would be described by the following Hamiltonian:

$$H = \sum_{i,j,m,m'\sigma} t_{i,j}^{m,m'} c_{im\sigma}^\dagger c_{jm'\sigma} - J \sum_{i,m} \left[ S_{i,d_{xy}}^z (c_{im\uparrow}^\dagger c_{im\uparrow} - c_{im\downarrow}^\dagger c_{im\downarrow}) + \frac{1}{2} (S_{i,d_{xy}}^+ c_{im\downarrow}^\dagger c_{im\uparrow} + S_{i,d_{xy}}^- c_{im\downarrow}^\dagger c_{im\uparrow}) \right]. \quad (15)$$

The first term denotes the hopping of the conduction electrons between the NN sites  $i, j$  with a hopping matrix element  $t_{i,j}^{m,m'}$  between the  $d_{yz\pm zx}$  orbitals, described by the  $m, m'$  indices. The  $d_{yz\pm zx}$  electrons and the localized  $d_{xy}$  spins interaction is given by the second term as an exchange coupling ( $J < 0$  for antiferromagnetic and  $J > 0$  for ferromagnetic coupling). The ferromagnetic coupling between the core spins and conduction electrons, favors ferromagnetic ordering, because the hopping amplitudes of the conduction electrons reach the maximum possible values if the core spins are aligned. Many of the Mn-type colossal magnetoresistance materials (CMR) can be described by such a model. Recently a realistic LDA+DMFT calculation for such a model is carried out.<sup>57</sup> The  $d$  shell of the  $\text{Mn}^{3+}$  in the undoped antiferromagnetic insulator contains three electrons in the  $t_{2g}$  orbitals forming a core spin of magnitude  $S = 3/2$ , which due to strong Hund's rule coupling couples ferromagnetically to one additional electron in one of the  $e_g$  orbitals. For a certain doping CMR materials are ferromagnetic metals because of additional holes in the  $e_g$  conduction bands.

In contrast to the manganites, in  $\text{CrO}_2$ , the  $d_{xy}$  spin has a smaller value  $S = 1/2$ , and the splitting of the localized  $d_{xy}$  orbital with respect to the itinerant  $d_{yz\pm zx}$  one is smaller [ $\approx 370$  meV, see. Eq. (12)].

It was shown recently<sup>58</sup> that for a proper definition of the many-body green function in  $\text{CrO}_2$ , the complete  $t_{2g}$  manifold is required. Moreover a better description of polarization can be obtained considering the competition between quasiparticle description around the Fermi level, and a local moment behavior at higher energies, above the Fermi level.<sup>58</sup>

According to our results, NMTO can give a minimal model with a possibly minimal set of distinct Wannier  $d_{xy}$  and  $d_{yz\pm zx}$  functions. This result does not exclude

the possibility of integrating out the degrees of freedom connected to the narrow/extended  $d_{xy}/d_{yz\pm zx}$  orbitals. Physically this would correspond to the dualistic character of the electronic structure of  $\text{CrO}_2$  around the Fermi level.<sup>59</sup>

### III. EFFECTIVE COULOMB REPULSION

The other essential component for a model Hamiltonian describing correlations, is the average Coulomb interaction parameter  $U$ . This term acts on the diagonal part of the effective Hamiltonian and corresponds to the screened electron-electron repulsion. Aryasetiawan *et al.* pointed out recently<sup>60</sup> that a rigorous way to define this quantity can be formulated in terms of path integrals by performing a partial trace, over the degrees of freedom, that one wants to eliminate. However, in practice for realistic materials, the elimination of degrees of freedom is a very difficult procedure.

In order to evaluate the average Coulomb interaction on the  $d$  atoms and the corresponding exchange interactions we start with the constrained LDA method.<sup>61,62,63,64,65,66</sup> In this approach the Hubbard  $U$  is calculated from the total energy variation with respect to the occupation number of the localized orbitals. In such a scheme the metallic screening is rather inefficient for  $3d$  transition metals.<sup>66</sup> The perfect metallic screening will lead to a smaller value of  $U$ . Unfortunately, there are no reliable schemes to calculate  $U$  in metals,<sup>67</sup> therefore in our previous works<sup>23,24,25,26</sup> we choose some intermediate values of  $U$  from 2 to 4.8 eV and  $J = 0.9$  eV.

In the case of  $\text{NiMnSb}$  the constrained LDA calculation indicates that the average Coulomb interaction between the Mn  $3d$  electrons is about  $U = 4.8$  eV with an exchange interaction energy about  $J = 0.9$  eV as seen in Table II. A reduced value of  $U$  can be obtained if one considers that the Mn  $e_g$  orbitals participate in the screening of Mn  $t_{2g}$ ,<sup>68,69</sup> reducing the average Coulomb interaction on the Mn atoms to a value of  $U = 4.2$  eV. However, our DMFT results<sup>23</sup> showed that the many-body effects are equally essential for  $t_{2g}$  and  $e_g$  orbitals, therefore a model with only Mn  $t_{2g}$ , even it may capture the main physical results, would suffer of incompleteness. Note that physical results for  $\text{NiMnSb}$  are not very sensitive to the value of  $U$ , as it was demonstrated.<sup>23</sup>

TABLE II: The constrained LDA values of the average Coulomb and exchange interactions. The second row corresponds to the results when the  $e_g$  orbitals screen the  $t_{2g}$  ones. This type of screening would be more appropriate for the  $\text{CrO}_2$  case.

	NiMnSb		CrO <sub>2</sub>	
	$U$ (eV)	$J$ (eV)	$U$ (eV)	$J$ (eV)
$t_{2g}$ and $e_g$	4.80	0.93	3.50	0.90
$t_{2g}$	4.25	0.93	3.00	0.87

Concerning the local Coulomb interaction  $U$ , in  $\text{CrO}_2$ , we saw from the analysis of the Cr- $3d$  manifold that the higher energy  $e_g$  bands makes no noticeable contribution to the Fermi level, however they could participate in the screening of the  $t_{2g}$  orbitals,<sup>68,69</sup> giving the following values for  $U=3$  eV and  $J=0.87$  eV.

### IV. SUMMARY

Spintronics requires the search for new materials such as half-metallic ferromagnets, whose properties are commanded by their electronic structure and electron-electron correlations. To understand the collective effects a clear picture of the interplay between the microscopic interactions is necessary. Model Hamiltonians allow a controlled reduction of the *ab initio* information into a few dominant material specific hopping and interaction parameters. In this paper we have applied the downfolding procedure within the  $N$ th order muffin-tin orbital (NMO) method to obtain model Hamiltonian parameters for two ferromagnetic half metals  $\text{NiMnSb}$  and  $\text{CrO}_2$ .

For  $\text{NiMnSb}$ , the present Wannier orbital results confirm the previous conclusions of Ref. [4] based on the gamma point analysis. However based on the whole Brillouin zone analysis we found that  $d$ - $d$  hybridization between the transition metal atoms is essential for the gap formation as the  $p$ - $d$  hybridization previously discussed.<sup>4</sup> Due to the significant Mn exchange splitting, a different hybridization takes place in the spin-up and spin-down channels, which determines the appearance of the gap only for spin-down electrons meanwhile for spin-up states a metallic character is evidenced.

A downfolding calculation which would include the Sb- $p$  and Ni- $d$  orbitals, would increase considerably the computational demand. However, the physical picture would not be very much changed, because an antibonding Mn  $d$  Wannier orbital including Sb  $p$  and Ni  $d$  character as a tail should play an important role for half-metallic nature around Fermi level. Therefore, the effective Hamiltonian described by Eqs. (4)–(6), represents a good starting point to investigate many-body effects.

Accordingly many-body correlation effects would be of primary importance for the Mn orbitals the Ni one could be neglected. In our previous many-body results<sup>23,24</sup> we made use of the above conclusions, so correlation effects were considered only for Mn- $d$  orbitals. The LDA+DMFT results showed the existence of non-quasiparticle states (NQP) state<sup>27,28</sup> in the minority spin channel. These states are associated with finite temperature spin fluctuation processes which play an important role in depolarization. In the majority spin channel,  $\text{FeMnSb}$  (Ref. 24) has a larger DOS at the Fermi level in comparison with  $\text{NiMnSb}$ .<sup>23</sup> This contributes to a stronger finite temperature depolarization in  $\text{FeMnSb}$ , which increase with the on-site Coulomb interaction.

For  $\text{CrO}_2$  the bands around the Fermi level are primarily chromium  $3d$  states of  $t_{2g}$  manifold, with  $e_g$  bands

situated higher in energy by the crystal-field splitting. The  $t_{2g}$  orbitals are further splitted into a single  $d_{xy}$  and nearly degenerate  $d_{yz\pm zx}$  bands due to the orthorhombical distortion of  $\text{CrO}_6$  octahedra. We discussed the direct and the mediated Cr- $d$ , O- $p$ , or Cr  $t_{2g}$ - $e_g$  interactions. Despite the differences between Cr  $t_{2g}$ - $e_g$  orbitals their interaction play an important role not only in characterizing the crystal-field splitting, but also in the general picture of bonding in the rutile structure.

The basis set of the Wannier orbitals for  $\text{CrO}_2$  is formed in  $t_{2g}$  manifold. In the framework of the NMTO technique two distinct downfolding procedures are possible.

In the first approach a full  $t_{2g}$  construction is possible, i.e., a single  $d_{xy}$  and a nearly degenerate  $d_{yz\pm zx}$  orbitals represents the basis set. We believe that such a basis set can be used in connection with the multiorbital Hubbard Hamiltonian described in Eq. (1).

A second approach is made possible due to a weak  $d_{xy}$  and  $d_{yz\pm zx}$  coupling. In this case the lowest  $d_{xy}$  and the higher  $d_{yz\pm zx}$  bands can be derived separately as shown in Fig. 10. For such a situation, downfolded NMTO

Hamiltonian with a set of those Wannier orbitals  $\{d_{xy}\}$  and  $\{d_{yz+zx}, d_{yz-zx}\}$ , is block diagonal, that is, there is no hopping between the lowest  $d_{xy}$  and the higher  $d_{yz\pm zx}$  orbitals. This fact gives a strong impression for a Kondo-lattice type model Hamiltonian described by Eq. (15). In a future work we report on the qualitative/quantitative differences of such models applied to  $\text{CrO}_2$ .

Similarly to our previous DMFT results on semi-Heuslers<sup>23,24</sup> and zinc-blende structures,<sup>25,26</sup> further work will include the many body effects in  $\text{CrO}_2$  and the analysis of nature of the NQP states in these classes of half-metallic ferromagnets.

## Acknowledgments

We are grateful for enlightening discussions with R.A. de Groot, O. Jepsen, O. Gunnarsson, K. Held, and E. Arrigoni. L.C. acknowledges financial support offered by the Austrian Science Foundation FWF Project No. P18505-N16.

- 
- \* Electronic address: A.Yamasaki@fkf.mpg.de
- <sup>1</sup> V. Yu. Irkhin and M. I. Katsnelson, *Usp. Fiz. Nauk* **164**, 705 (1994) [*Phys. Usp.* **37**, 659 (1994)].
  - <sup>2</sup> S. A. Wolf, D. D. Awschalom, R. A. Buhrman, J. M. Daughton, S. von Molnár, M. L. Roukes, A. Y. Chtchelkanova, and D. M. Treger, *Science* **294**, 1488 (2001).
  - <sup>3</sup> I. Žutić, J. Fabian, and S. Das Sarma, *Rev. Mod. Phys.* **76**, 323 (2004).
  - <sup>4</sup> R.A. de Groot, F.M. Mueller, P.G. van Engen, and K.H.J. Buschow, *Phys. Rev. Lett.* **50**, 2024 (1983).
  - <sup>5</sup> R. J. Soulen, Jr., M. Byers, M. S. Osofsky, B. Nadgorny, T. Ambrose, S. F. Cheng, P. R. Broussard, C. T. Tanaka, J. Nowak, J. S. Moodera, A. Barry, and J. M. D. Coey, *Science* **282**, 85 (1998); R. J. Soulen, Jr., M. S. Osofsky, B. Nadgorny, T. Ambrose, P. Broussard, S. F. Cheng, J. M. Byers, C. T. Tanaka, J. Nowack, J. S. Moodera, G. Laprade, A. Barry, and M. D. Coey, *J. Appl. Phys.* **85**, 4589 (1999).
  - <sup>6</sup> S. K. Clowes, Y. Miyoshi, Y. Bugoslavsky, W. R. Branford, C. Grigorescu, S. A. Manea, O. Monnereau, and L. F. Cohen, *Phys. Rev. B* **69**, 214425 (2004).
  - <sup>7</sup> W. Zhu, B. Sinkovic, E. Vescovo, C. Tanaka, and J. S. Moodera, *Phys. Rev. B* **64**, 060403(R) (2001).
  - <sup>8</sup> M. Sicot, P. Turban, S. Andrieu, A. Tagliaferri, C. De Nadai, N. B. Brookes, F. Bertran, and F. Fortuna, *J. Magn. Magn. Mater.* **303**, 54 (2006).
  - <sup>9</sup> G. A. de Wijs and R. A. de Groot, *Phys. Rev. B* **64**, 020402(R) (2001).
  - <sup>10</sup> Y. Ji, G. J. Strijkers, F. Y. Yang, C. L. Chien, J. M. Byers, A. Anguelouch, G. Xiao, and A. Gupta, *Phys. Rev. Lett.* **86**, 5585 (2001).
  - <sup>11</sup> J. S. Parker, S. M. Watts, P. G. Ivanov, and P. Xiong, *Phys. Rev. Lett.* **88**, 196601 (2002).
  - <sup>12</sup> Y.S. Dedkov, M. Fonine, C. Konig, U. Rudiger, G. Guntherodt, S. Senz, and D. Hesse, *Appl. Phys. Lett.* **80**, 4181 (2002).
  - <sup>13</sup> J.M.D. Coey, J. Versluijs, and M. Venkatesen, *J. Phys. D* **35**, 2457 (2002).
  - <sup>14</sup> R. S. Keizer, S. T. B. Goennenwein, T. M. Klapwijk, G. Miao, G. Xiao, and A. Gupta, *Nature (London)* **439**, 825 (2006).
  - <sup>15</sup> A. I. Lichtenstein and M. I. Katsnelson, *Phys. Rev. B* **57**, 6884 (1998).
  - <sup>16</sup> W. Metzner and D. Vollhardt, *Phys. Rev. Lett.* **62**, 324 (1989).
  - <sup>17</sup> A. Georges, G. Kotliar, W. Krauth, and M. Rozenberg, *Rev. Mod. Phys.* **68**, 13 (1996).
  - <sup>18</sup> V. I. Anisimov, A. I. Poteryaev, M. A. Korotin, A. O. Anokhin, and G. Kotliar, *J. Phys.: Condens. Matter* **9**, 7359 (1997).
  - <sup>19</sup> M. I. Katsnelson and A. I. Lichtenstein, *J. Phys.: Condens. Matter* **11**, 1037 (1999).
  - <sup>20</sup> K. Held, I. A. Nekrasov, G. Keller, V. Eyert, N. Blümer, A. K. McMahan, R. T. Scalettar, Th. Pruschke, V. I. Anisimov, and D. Vollhart, *Psi-k Newsletter #56*, 65 (2003) [[http://psi-k.dl.ac.uk/newsletters/News\\_56/Highlight\\_56.pdf](http://psi-k.dl.ac.uk/newsletters/News_56/Highlight_56.pdf)].
  - <sup>21</sup> L. Chioncel, L. Vitos, I. A. Abrikosov, J. Kollár, M. I. Katsnelson, and A. I. Lichtenstein, *Phys. Rev. B* **67**, 235106 (2003).
  - <sup>22</sup> G. Kotliar and D. Vollhardt, *Phys. Today* **57**, 53 (2004); G. Kotliar, S. Y. Savrasov, K. Haule, V. S. Oudovenko, O. Parcollet, and C.A. Marianetti, to be published in *Rev. Mod. Phys.* **78** (2006), cond-mat/0511085.
  - <sup>23</sup> L. Chioncel, M. I. Katsnelson, R. A. de Groot, and A. I. Lichtenstein, *Phys. Rev. B* **68**, 144425 (2003).
  - <sup>24</sup> L. Chioncel, E. Arrigoni, M.I. Katsnelson, and A.I. Lichtenstein, *Phys. Rev. Lett.* **96**, 137203 (2006).
  - <sup>25</sup> L. Chioncel, M. I. Katsnelson, G. A. de Wijs, R. A. de Groot, and A. I. Lichtenstein, *Phys. Rev. B* **71**, 085111 (2005).

- <sup>26</sup> L. Chioncel, Ph. Mavropoulos, M. Ležaić, S. Blügel, E. Arriagón, M.I. Katsnelson, and A.I. Lichtenstein, *Phys. Rev. Lett.* **96**, 197203 (2006).
- <sup>27</sup> D. M. Edwards and J. A. Hertz, *J. Phys. F* **3**, 2191 (1973).
- <sup>28</sup> V. Yu. Irkhin and M. I. Katsnelson, *Fizika Tverdogo Tela* **25**, 3383 (1983) [*Sov. Phys. - Solid State* **25**, 1947 (1983)]; *J. Phys. : Condens. Matter* **2**, 7151 (1990).
- <sup>29</sup> B. Sanyal, L. Bergqvist, and O. Eriksson, *Phys. Rev. B* **68**, 054417 (2003).
- <sup>30</sup> O. K. Andersen and T. Saha-Dasgupta, *Phys. Rev. B* **62**, R16219 (2000); O. K. Andersen, O. Jepsen, and G. Krier, in *Methods of Electronic Structure Calculations*, edited by V. Kumar, O. K. Andersen, and A. Mookerjee (World Scientific, Singapore, 1994), pp. 63–124; O. K. Andersen, T. Saha-Dasgupta, R. W. Tank, C. Arcangeli, O. Jepsen, and G. Krier, in *Electronic Structure and Physical Properties of Solids. The Uses of the LMTO Method*, edited by H. Dreyse, Springer Lecture Notes in Physics (Springer, New York, 2000), pp. 3–84; O. K. Andersen, T. Saha-Dasgupta, S. Ezhov, L. Tsetseris, O. Jepsen, R. W. Tank, C. Arcangeli, and G. Krier, *Psi-k Newsletter* #45, 86 (2001) [[http://psi-k.dl.ac.uk/newsletters/News\\_45/Highlight\\_45.pdf](http://psi-k.dl.ac.uk/newsletters/News_45/Highlight_45.pdf)].
- <sup>31</sup> E. Zurek, O. Jepsen, and O. K. Andersen, *ChemPhysChem* **6**, 1934 (2005).
- <sup>32</sup> O. K. Andersen, *Phys. Rev. B* **12**, 3060 (1975).
- <sup>33</sup> O. K. Andersen and O. Jepsen, *Phys. Rev. Lett.* **53**, 2571 (1984).
- <sup>34</sup> The Stuttgart TB-LMTO-ASA code, version 4.7. See: <http://www.fkf.mpg.de/andersen/>.
- <sup>35</sup> E. Pavarini, A. Yamasaki, J. Nuss, and O. K. Andersen, *New J. Phys.* **7**, 188 (2005).
- <sup>36</sup> S. Ögüt and K. M. Rabe, *Phys. Rev. B* **51**, 10443 (1995).
- <sup>37</sup> I. Galanakis, P. H. Dederichs, and N. Papanikolaou, *Phys. Rev. B* **66**, 134428 (2002).
- <sup>38</sup> B. R. K. Nanda and I. Dasgupta, *J. Phys.: Condens. Matter* **15**, 7307 (2003).
- <sup>39</sup> E. Kulatov and I. I. Mazin, *J. Phys.: Condens. Matter* **2**, 343 (1990).
- <sup>40</sup> B.J. Thamer, R.M. Douglass, and E. Staritzky, *J. Am. Chem. Soc.* **79**, 547 (1957).
- <sup>41</sup> S.P. Lewis, P.B. Allen and T. Sasaki, *Phys. Rev. B* **55**, 10253 (1997).
- <sup>42</sup> M.A. Korotin, V.I. Anisimov, D.I. Khomskii, and G.A. Sawatzky, *Phys. Rev. Lett.* **80**, 4305 (1998).
- <sup>43</sup> P. Schlottmann, *Phys. Rev. B* **67**, 174419 (2003).
- <sup>44</sup> B.L. Chamberland, *CRC Crit. Rev. Solid State Mater. Sci.* **7**, 1 (1977).
- <sup>45</sup> T. Tsujioka, T. Mizokawa, J. Okamoto, A. Fujimori, M. Nohara, H. Takagi, K. Yamaura, and M. Takano, *Phys. Rev. B* **56**, R15509 (1997).
- <sup>46</sup> C.B. Stagescu, X. Su, D. E. Eastman, K. N. Altmann, F. J. Himpsel, and A. Gupta, *Phys. Rev. B* **61**, R9233 (2000).
- <sup>47</sup> K. Suzuki and P. M. Tedrow, *Phys. Rev. B* **58**, 11597 (1998).
- <sup>48</sup> E.J. Singley, C. P. Weber, D. N. Basov, A. Barry, and J. M. D. Coey, *Phys. Rev. B* **60**, 4126 (1999).
- <sup>49</sup> K.H. Schwarz, *J. Phys. F* **16**, L211 (1986).
- <sup>50</sup> I.I. Mazin, D.J. Singh, and C. Ambrosch-Draxl, *Phys. Rev. B* **59**, 411 (1999).
- <sup>51</sup> M.S. Laad, L. Craco, and E. Muller-Hartmann, *Phys. Rev. B* **64**, 214421 (2001); L. Craco, M.S. Laad, and E. Muller-Hartmann, *Phys. Rev. Lett.* **90**, 237203 (2003).
- <sup>52</sup> P. I. Sorantin and K. Schwarz, *Inorg. Chem.* **31**, 567 (1992).
- <sup>53</sup> Note that the local coordinate system in the paper Ref. [52] is different from the one presented in Ref. [42]. In the present paper we use the convention presented in the later Ref. [42].
- <sup>54</sup> P. Porta, M. Marezio, J. P. Remeika, and P. D. Dernier, *Mater. Res. Bull.* **7**, 157 (1972).
- <sup>55</sup> T. Saha-Dasgupta, O. K. Andersen, J. Nuss, A. Poteryaev, A. I. Lichtenstein, and A. Georges (unpublished).
- <sup>56</sup> O. K. Andersen, I. I. Mazin, O. Jepsen, M. D. Johannes, and A. Yamasaki (unpublished).
- <sup>57</sup> A. Yamasaki, M. Feldbacher, Y. -F. Yang, O. K. Andersen, and K. Held, *Phys. Rev. Lett.* **96**, 166401 (2006).
- <sup>58</sup> M. van Veenendaal and A. J. Fedro, *Phys. Rev. B* **70**, 012412 (2004).
- <sup>59</sup> D. J. Huang, L. H. Tjeng, J. Chen, C. F. Chang, W. P. Wu, S. C. Chung, A. Tanaka, G. Y. Guo, H.-J. Lin, S. G. Shyu, C. C. Wu, and C. T. Chen, *Phys. Rev. B* **67**, 214419 (2003).
- <sup>60</sup> F. Aryasetiawan, M. Imada, A. Georges, G. Kotliar, S. Biermann, and A. I. Lichtenstein, *Phys. Rev. B* **70**, 195104 (2004).
- <sup>61</sup> P. H. Dederichs, S. Blügel, R. Zeller, and H. Akai, *Phys. Rev. Lett.* **53**, 2512 (1984).
- <sup>62</sup> M. R. Norman and A. J. Freeman, *Phys. Rev. B* **33**, R8896 (1986).
- <sup>63</sup> A. K. McMahan, R. M. Martin, and S. Satpathy, *Phys. Rev. B* **38**, 6650 (1988).
- <sup>64</sup> O. Gunnarsson, O. K. Andersen, O. Jepsen, and J. Zaanen, *Phys. Rev. B* **39**, 1708 (1989).
- <sup>65</sup> M. S. Hybertsen, M. Schlüter, and N. E. Christensen, *Phys. Rev. B* **39**, 9028 (1989).
- <sup>66</sup> V. I. Anisimov and O. Gunnarsson, *Phys. Rev. B* **43**, 7570 (1991).
- <sup>67</sup> For recent progress, see Ref. [60]; I. V. Solovyev and M. Imada, *Phys. Rev. B* **71**, 045103 (2005); F. Aryasetiawan, K. Karlsson, O. Jepsen, and U. Schönberger, *cond-mat/0603138*.
- <sup>68</sup> I. Solovyev, N. Hamada, and K. Terakura, *Phys. Rev. B* **53**, 7158 (1996).
- <sup>69</sup> W. E. Pickett, S. C. Erwin, and E. C. Ethridge, *Phys. Rev. B* **58**, 1201 (1998).